Drag mitigation by steady blowing and Coanda effect on a square back Ahmed body

Baptiste Plumejeau, Laurent Keirsbulck, Jérémy Basley, Marc Lippert, Sébastien Delprat, Wafik Abassi

Drag mitigation by steady blowing and Coanda effect on a square back Ahmed body

Baptiste Plumejeau,[1,2] Laurent Keirsbulck,[1] Jérémy Basley,[1,a)] Marc Lippert,[1] Sébastien Delprat,[1] and Wafik Abassi[2]
[1)]LAMIH, CNRS UMR 8201, *Le Mont Houy, 59300 Valenciennes, France*
[2)]IPSA, *63 Boulevard de Brandebourg, 94200 Ivry-sur-Seine, France*

(Dated: 5 December 2024)

The impact of converging steady blowing on the global drag past a square back Ahmed bluff body is investigated experimentally. The dynamics of the recirculation bubble are studied for a width to height aspect ratio, w/h of 1.346, with a ground clearance of $g/w = 0.154$, and for a nominal Reynolds number of $Re_h = 2.86\times10^5$. When unforced, the bistable wake alternates between a left and right skewed states. Adaptable Coanda devices are used in combination with side air-knife blowers to deflect steady blowing jets into a converging (boat-tail) configuration. Two yaw angles are investigated: 45° and 90°. Planar PIV and time-history force and pressure measurements indicate that inwards steady blowing reshapes the recirculation bubbles and induces significant variations of the pressure drag. On one hand, bilateral steady blowing leads to the interruption of bistability associated with a removal of the vertical pressure gradient for velocity ratios $V_R \approx 0.35 - 0.4$. This has a favourable impact on the total drag with a reduction up to 3%. On the other hand, the boat-tailing effect shortens the recirculation length which tends to increase drag. This counter-productive effect limits and then outweighs drag reduction for higher velocity ratios. Another symmetry breaking is brought to light for intense highly deflected forcing.

Keywords: Active flow control, Coanda effect, steady blowing, square-back Ahmed body, wake symmetry breaking

I. INTRODUCTION

In land transportation, intelligent systems are an increasingly important research field. Innovative systems are emerging through numerous applications such as autonomous vehicles. In this context, flow control gives us a real perspective in terms of consumption reduction and manoeuvrability improvement of aerodynamic systems. Many works on the flow control of simplified vehicle models (car[1,2], truck[3]) show a way of improvement for the road transportation. The wake dynamics of bluff bodies is still subject of recent research since the recirculating bubble itself is absolutely unstable and highly receptive to external perturbations such as steady blowing or jet flow oscillations. Consequently, flow control turned out to be an efficient way to increase the bluff body wakes base pressure distribution. Extensive investigations over the years show that a drag reduction is associated with a weakening of the wake vortex strength or to a backward movement of low pressure areas corresponding to the vortex cores.

For bluff bodies with very high or low width to height aspect ratio, w/h (2D flows), the closest shear layers interact strongly with each other, which leads to the well-known vortex shedding (global mode). Since this phenomenon induces high amplitude fluctuation very close to the base of the body, its impact on the pressure base is predominant. As a result, the most efficient control strategy for these configurations is to mitigate this quasi-periodic vortex shedding mode[4]. The inhibition of the strong periodic dynamics can be achieved by reducing the wake dynamics activity using splitter plates (central[5] or lateral[6]), side slit jets[7] or base bleed[8].

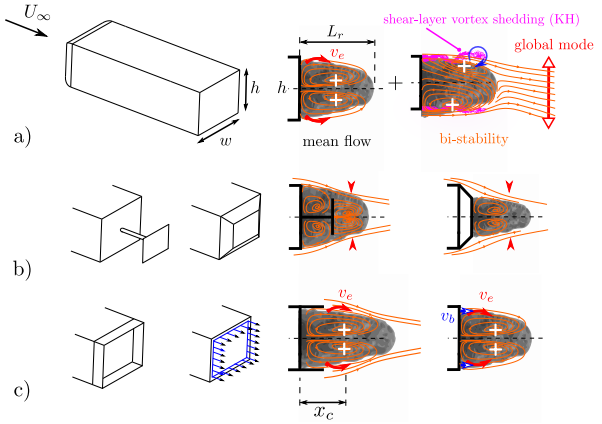

FIG. (1) Main mechanisms used for drag reduction of bluff bodies with a 3D flow behaviour (typically with $w/h \approx [0.5, 1.5]$); (a) uncontrolled flow, mean and instantaneous flows, (b) Base parallel splitter plate and boat-tail (mean flow), (c) Base cavity and steady sides blowing (mean flow).

For 3D bluff body flows (see FIG.1, with L_r denotes the mean length of the recirculation bubble and v_e denotes the entrainment velocity of the shear-layer), the goal is similar, but since the global mode are

[a)]Electronic mail: jeremy.basley@uphf.fr

not in the same order of amplitude compared to the previous 2D flows, the control strategies are quite different. In addition to the complexity induced by the three-dimensionality, additional static global modes[9–11] due to ground proximity leads to an asymmetry of the wake flow vortex positions. Therefore, one of the primary goals of control strategies becomes the recovery of wake symmetry, in particular in the low pressure area (by feedback flow control[12–14] strategies for example). Another objective is to reduce the cross section of the wake (so-called wake shaping). The last one is to increase the recirculation length by reducing the entrainment velocity. In the past, the base parallel splitter plates[15] and boat tails[16] are known to be efficient to reduce the cross section of the wake. Concerning the strategies allowing the reduction of entrainment, various possibilities can be considered. The base cavity[17–19] generates an elongation of the recirculation inside the cavity that considerably attenuates the low pressure sources compared to the natural case. This is mainly due to the starting point of external entrainment of the fluid inside the recirculation region being pushed further away from the corner edge of the body (see Fig.1c). That is essentially why results obtained with steady blowing do not appear transferable in terms of drag reduction to those obtained for the base cavity. High frequency periodic forcing through side slits[20–22] has also demonstrated its effectiveness, first by inducing a deviation of the separated shear layer, and secondly by reducing the entrainment towards the recirculating bubble. The combination of both mechanisms produces a raise of the base pressure and reduces the global drag of the model. In the other forcing actuation cases (broadband or low frequency), the convection of the jet structures enhances wake entrainment, shortens the length of the recirculating bubble and increases drag systematically.

Recently, Lorite-Díez *et al.*[23] have investigated the case of streamwise steady blowing. They analysed the effect of local base blowing on three-dimensional wake modes and clearly identified two regimes referred to as mass and momentum. On the one hand, the *mass regime* is characterised by the moderate blowing ratio that feeds the recirculating bubble but whose momentum is dissipated (low effect on the entrainment velocity) leading to an inflation of the recirculating length. On the other hand, the *momentum regime*, obtained for higher blowing ratio, enhances the entrainment velocity from the shear layers, which deflates the recirculating bubble and reduces the recirculating length. The authors interpreted the phenomenon as an equilibrium between mass fluxes feeding and emptying the recirculating bubble. This work has also brought to light that symmetric blowing attenuates the static asymmetric mode in the mass regime. This offers interesting perspectives in better understanding the mechanisms underlying flow control. Building on the approach of the so-called

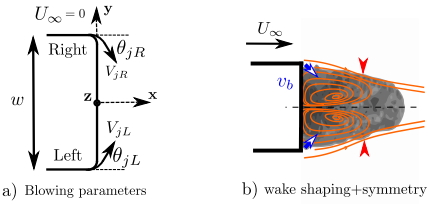

FIG. (2) Present steady blowing configurations and strategy to suppress the bistability and shaping the wake in the case of bilateral blowing.

mass regime, latest works by O. Cadot, L. Pastur, and Parezanović and their co-authors localise the forcing directly inside the bubble rather than on the edges, to affect the static modes directly. Drag reduction is obtained using pulsed jets[24,25], or suction rather than blowing[26]. Both strategies aim to deplete the static modes, either by enhancing high-frequency modes or by reducing the mass flux into the bubble.

At the same time, Haffner and co-authors proposed in-depth investigations of the reconfiguration of the recirculating bubble. First, in Haffner *et al* 2020[27] the natural transient dynamics of the bubble between asymmetric states was identified and related to a drag reduction, as both vortex cores are simultaneously further from the body. Then, Haffner *et al* 2021[28] achieved the manipulation of the recirculation bubble using a variety of streamwise side-slit blowing configurations (top, bottom, left, right and all possible combinations). They characterised the reconfiguration of the recirculating bubble and the corresponding drag alteration, depending on the location of the side-slit blowing, symmetric or not.

The present study builds on these recent findings yet focuses on an alternative forcing using Coanda effect to deviate the injection of momentum from the natural streamwise driving force (see Fig.2). Inclining air-knife jets inwards aims to emulate the highly effective influence of boat-tail geometries on the recirculation bubble, without the added mass and viscous drag. Coanda effect was used recently by Haffner *et al* 2020[22] but with pulsed jets to target interactions with the vortex-shedding of the external shear layers. Note that air knife blowers are located at the left and right edges to provide further lateral control of the recirculation regions. This accounts for the aspect ratio known to induce a lateral bistability (as demonstrated in Grandemange *et al.*[11]). The outline of the paper is as follows. The experimental set-up is detailed in §II. The results of the steady blowing control are described in §III. A scenario explaining the mechanisms that underlie the evolution of the drag is proposed in §IV, before concluding remarks in §V.

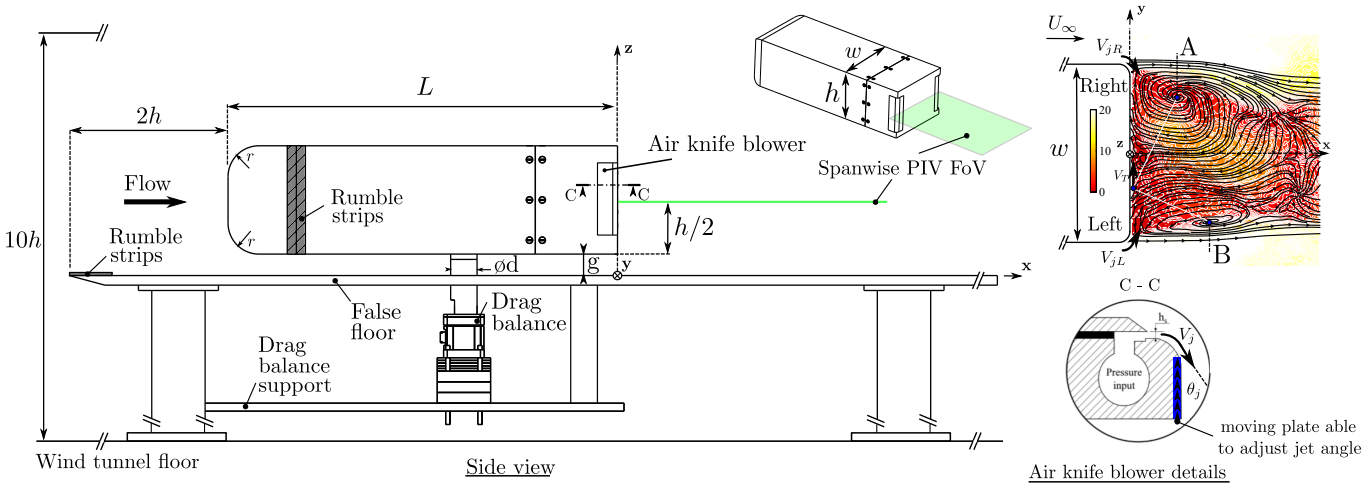

FIG. (3) Side and 3D views of the experimental setup, showing the spanwise PIV field of view and the locations of the side blowers. Bottom right corner, a close-up cross-view of the adjustable Coanda device designed to modify the blowing jet angle, θ_j. Top right corner, an instantaneous flow field includes the two main wake vortex cores denoted by **A** and **B** and the tangential velocity, V_T close to the back of the Ahmed body, and colours represent the velocity magnitude.

II. EXPERIMENTAL CONFIGURATION

This section describes the experimental rig and the bluff body arrangement. The different measurement techniques are presented and the forcing jet produced by the actuation device is characterised in all investigated configurations.

A. Wind-tunnel facility and instrumented Ahmed body

The experimental campaign was performed in a closed-loop subsonic wind-tunnel with a 6.25:1 contraction ratio. The 10m-long working section has a $2 \times 2\text{m}^2$ cross-sectional area and the free-stream turbulent intensity is less than 0.6%. The Ahmed body model shown in FIG.3 was centred between the side walls, the ceiling, and the floor within the test section. The geometry was placed in wall proximity with a plate up raised above the floor within the test section. The coordinate system is defined as (x,y,z) in the streamwise, spanwise, wall-normal directions, respectively, as shown in FIG.3. The bluff body has a width, w of 272mm and a height, h of 202mm, leading to an aspect ratio, w/h of 1.346, and a length, L of 730mm, and the radius of the rounding of the fore-body is $r = 29$mm. In the following, dimensionless coordinates are defined using h such that $(x^*, y^*, z^*) =$(x,y,z)$/h$. The cylindrical central support has a diameter of $d = 50$mm. The ground clearance is set to $g = 42$mm. The model corresponds to the original Ahmed body[1] configuration with a scale of 0.7. In order to thicken the turbulent boundary layer, a 35mm wide strip is installed at the beginning of the flat plate and on the front part of the Ahmed body. Based on the height of the model, the Reynolds number of this flow is defined as $Re_h = U_\infty.h/\nu$, where ν is the kinematic viscosity of the air at ambient temperature and U_∞ the free-stream velocity. Experiments are conducted at a free-stream velocity of $U_\infty = 20$m/s, corresponding to $Re_h = 2.86 \times 10^5$.

B. Force, pressure, and velocity measurements

The total drag and side force coefficients C_D and C_y, respectively, are defined by $C_D = F_x/(S.p_{dyn})$, and $C_y = F_y/(S.p_{dyn})$, where F_x and F_y are the measured drag and drift forces, $p_{dyn} = \frac{1}{2}\rho U_\infty^2$, with ρ the air density, and S the projected frontal body area. In order to quantify the total aerodynamic drag and drift forces, a 6-components DELTA ATI balance (MC-3A model 500) with a sensitivity of 1.35μV/V is used. A Dewesoft signal conditioner processes the raw sensor measurements with a resulting resolution estimated to ± 0.01N. Force measurements are low-pass filtered using a zero-phase digital filter. An extensive study of the reliability of time-resolved measurements from this aerodynamic balance was recently published in Lippert *et al.*[29]. Once low-pass filtered, aerodynamic time histories proved to be appropriate quality signals to investigate the simultaneous evolutions of drag and side force.

Thirty-five static pressure tabs are distributed on a 7×5 grid at the rear of the body separated by ($\delta y = 0.15h$ and $\delta y = 0.12h$). The static pressure is obtained using a 64 port miniature Scanivalve MPS4264 pressure scanner (effective measurement range of 2000Pa) with a static accuracy of $\pm 0.1\%$ fso corresponding to $\pm 3Pa$. The pressure scanner takes 20 pressure samples per second and per channel. The pressure scanner is located inside the model to limit the filtering effect of the vinyl tubing (shorter than 150mm to each tap). In the following, the pressure coefficient is calculated by $C_p(y^*, z^*, t^*) = (p(y^*, z^*, t^*) - p_\infty)/p_{dyn}$, where p_∞ denotes the reference static pressure, measured in the test section at 1 m upstream from the model. Wake asymmetry is assessed by

using the dimensionless horizontal and vertical base pressure gradients, $g_y = \partial C_p/\partial y^*$ and $g_z = \partial C_p/\partial z^*$.

Particle Image Velocimetry (PIV) measurements are carried out with a standard two-component TSI system, composed of a double-pulse 200mJ dual-head ND-YAG (Quantel BSLT220) laser system and high-resolution CCD Powerview camera with a full resolution of 2048 × 2048 pixels and micro NIKKOR 50mm optical lens. The seeder is a TSI oil droplet atomizer 9307 whose droplets diameter's main mode is about $d_p = 1\mu$m. The seeding is released in the settling chamber of the wind tunnel. The vector fields are obtained by processing the PIV images using a recursive cross-correlation algorithm with a final interrogation window size of 16×16 pixels with 50% overlap leading to a spatial resolution of about 6.7 vectors/cm or 128 vectors/h. The uncertainty is estimated at 0.5% on the velocity and 2.5% on Ω_z for the worst considered cases. The resulting PIV fields of view passing through the spanwise middle planes of the Ahmed body are about $1.6h \times 2h$ (FIG.3). For every test case, 1000 time-uncorrelated PIV snapshots are recorded with a repetition rate of 7Hz. For tests without free-stream velocity, the wind tunnel having a closed return circuit, the flow was preventively seeded prior to data acquisition.

C. Control devices

The model is equipped with air-knife blowers at both left and right edges, as illustrated in FIG.3. The slit width is h_s=0.1mm, that is $0.0005h$, and the actuation length is w_a=150mm ($\approx 0.75h$) leading to a slit jet section $s_j = 15\text{mm}^2$. This device generates a focused air-knife jet characterised by peak velocity V_j, driven by FESTO-MH2 solenoid valves controlled by a trigger signal. The peak velocity V_j was measured in a calibration process detailed in §II D. The jets can be blown tangentially ($\theta_j = 90°$) or with an angle of $\theta_j = 45°$ to the rear surface of the body thanks to an adaptable Coanda rounded surface, as described in FIG.3. In the following, the control strength is estimated by the velocity ratio $V_R = \dfrac{V_j}{U_\infty}$. Note that another control parameter could be used: the flow rate coefficient $C_q = q_j/(hwU_\infty)$, whenever the blowing flow rate of the jet q_j can be determined.

D. Characterisation of the steady jets

This investigation delves into a range of steady blowing flow configurations, varying the blowing ratio and injection angles of $\theta_j = 45°$ or 90°. Bilateral and one-sided combinations are considered, i.e. right-hand side blowing only, left-hand side only, and air-blowing on both sides of the body. First, the different steady blowing combinations are investigated without free-stream velocity flow to characterise the jets, their expansion and their interaction with the geometry. In addition to the present spatial characterisation an in-depth hot-wire dynamic characterisation has already been published in Chovet *et al.*[30]). It was shown that the device used in conjunction with an adjustable rectangular plate enables various injection angles by deviating the jet without distortion.

TABLE (I) Steady blowing parameters of the ten forcing injections under study.

	$V_j(m/s)$	6	7	8	9	10
	V_R [a]	0.30	0.35	0.40	0.45	0.50
$\theta_j = 45°$	θ_{j_L}	45°	44°	45°	48°	45°
	θ_{j_R}	46°	45°	44°	47°	47°
	$(y/h)_{\text{L+R}}$ [b]	0.02	-0.04	-0.04	-0.05	-0.05
$\theta_j = 90°$	θ_{j_L}	87°	87°	88°	90°	89°
	θ_{j_R}	87°	88°	88°	89°	90°
	$(y/h)_{\text{L+R}}$	0.04	-0.05	-0.04	-0.02	-0.03

[a] Free-stream velocity is $U_\infty = 20$m/s
[b] Spanwise position of the impingement in the case of bi-lateral blowing jets

Examples of mean velocity fields obtained from PIV measurements are shown in FIG.4. Jet angle and amplitude are identified using velocity profiles extracted from mean flow fields for every PIV data set. The direction of the jet is characterised by following the maximum velocity peak leaving the Coanda device. The blowing ratio is obtained by tracking the maximum velocity close to the air-knife device. Results show very good consistency of the jet yaw angle for the various data sets, and only a few small discrepancies can be observed for the considered jet velocity range. In bilateral blowing cases FIG.4b and 4d, the mean flow without free-stream velocity exhibits symmetric jets consistent with the parameter θ_j. Remark however that the mean cannot represent the sweeping motion that inherently appears downstream where the two jets impinge onto each other. This behaviour will be briefly discussed for high velocity ratios in the last section of the discussion.

Preliminary visualisations (not shown here) have demonstrated the good homogeneity and stability of the jet along the slit span. The deflection of the jet is smooth down to 45° and no distortion is observed. For injection angles lower than 20°, the rectangular plate is very close to the exit of the jet. This causes strong disruptions of the jets, and the flow becomes significantly distorted. That is why angles from 0 to 20° cannot be investigated and directly compared to studies using streamwise injection from the literature.
Regarding the effect of velocity ratio, analyses reveal higher jet penetration and a larger jet expansion as the jet velocity is increased, as shown in FIG.4. Mean flow fields displayed in FIG.4a and 4c, show that one-sided blowing induces a cross wind movement. For an injection angle of 45°, additional vortex structures are observed close to the actuator (see FIG.4a and 4b). It is worth noting that the control parameter C_q is often preferred to

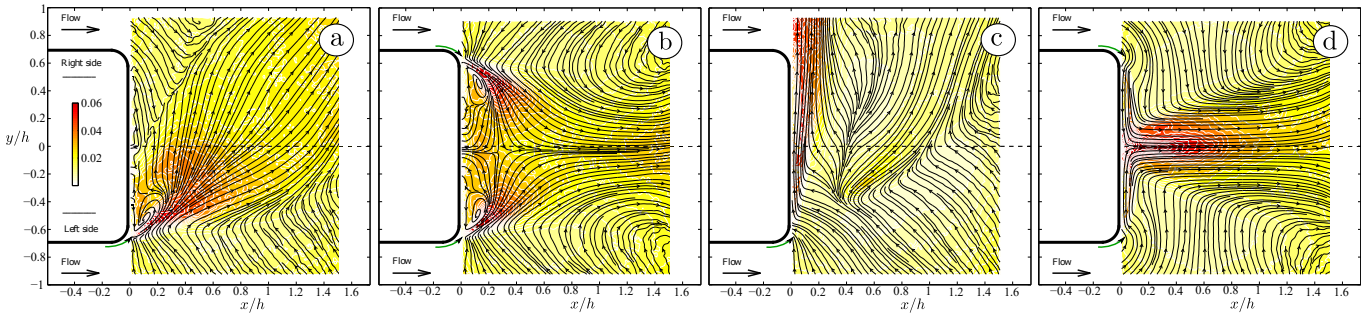

FIG. (4) Steamlines fields of some steady blowing configurations without free stream for $V_j = 8$ m/s. Contours denote RMS levels. Blowing at $\theta_j = 45°$ on left-hand side only (a), and bilateral (b). Blowing at $\theta_j = 90°$ on the left-hand side only (c), and bilateral (d).

V_R in recent studies investigating mass exchange with the recirculation region. However, the Coanda-effect devices used here have a particularly narrow slit ($h_s = 0.1$mm), which makes impossible estimating the mass flow rate. Indeed, while the velocity ratio is determined from the established jet, the mass flow rate requires a direct measurement of the outflow, an impracticable task in this case. The other solution was using a flowmeter in the supplied flow, but this was not available at the time of the experimental campaign.

On a side note, it is worth pointing out that lopsided blowing configurations, in which left and right jets are not equal, were investigated (not shown here). It can be inferred that any skewed forcing results in a asymmetric flow, not unlike that of a purely one-sided blowing case L or R. For the sake of brevity only the symmetric bilateral case (same velocity ratio on the left and right), the left-hand side only and the right-hand side only cases, are considered in the following. They are hereafter denoted by L+R, L and R, respectively.

III. RESULTS & DISCUSSION

A series of steady blowing configurations were tested to determine the effect that each combination of flow control parameters has on the total drag associated with velocity field alterations. By adjusting the inlet pressure of the actuator and the plate position (FIG.3), a range of velocity ratios (injection momentum) are obtained for two jet angles. Every case is reported in TAB. I. The parameters considered here are the jet yaw angle θ_j and the velocity ratio V_R. **TABLE I** shows that the jets are indeed symmetrical with angles of $45 \pm 3°$ and $90 \pm 3°$, respectively, for the various blowing ratios. In cases of bilateral blowing (L+R), the mirror plane is within 5% of the centreline of the body, emphasizing the good balance of the lateral jets.

A. Overview of the recirculating flow manipulation

FIG.5 gives an overview of the recirculating flow fields for some of the steady blowing cases with $\theta_j = 45°$ (L+R blowing cases on top, L blowing cases on the bottom line, for $V_R = \{0.3, 0.4, 0.5\}$). The baseline case is shown as reference with its total average and conditional average $\#N$ for the sake of comparison with the controlled cases. Bilateral blowing preserves the symmetry of the mean flow (FIG.5 top). Both vortex cores are brought closer to the rear of the body as blowing ratio increases. In contrast, when one-sided blowing is used (FIG.5 bottom for (L) blowing cases), the vortex closest to the jet is enhanced and migrates towards the centreline while the opposite smaller vortex moves slightly downstream. This reduces the recirculation bubble and heightens the asymmetry of the wake. In fact, the mean flow resembles the corresponding skewed state explored by the bistable regime of the baseline case at $V_R = 0$. These results are comparable to the cases of asymmetric forcing investigated by Haffner *et al* 2021[28]. It is worth noting that the destabilisation of the recirculation bubble, either obtained via flow control or by intrinsic symmetry breaking of the bistable state, strongly affects the pressure distribution of the base. There is also a strong relationship between the position of the vortex cores and the entrainment of the recirculation bubble due to their relative proximity with the shear layers resulting from the separated boundary layers[23,28].

The location of the main vortical cores is determined using the two-dimensional velocity field acquired from planar PIV. Since the highest levels of out-of-plane vorticity component, Ω_z, are exhibited by the shear layers developing around the wake region, vortex cores were identified by the Γ_1 criterion proposed by Graftieaux *et al.*[31]. They are marked by white circles in FIG.5. The peak vorticity of the vortex cores, Ω_0, is extracted from conditionally averaged flow fields, and plotted as a function of the vortex core spanwise position in FIG.6 for all investigated cases (TAB. I). The peak vorticity tends to be almost constant, equal to 1 around the $y/h = 0$ region but increases linearly with its spanwise position as the vortices get further from the centreline ($|y/h| > 0.3$), due to the overriding influence of the side shear layers. The collapse between $\theta_j = 45^o$ and 90^o data

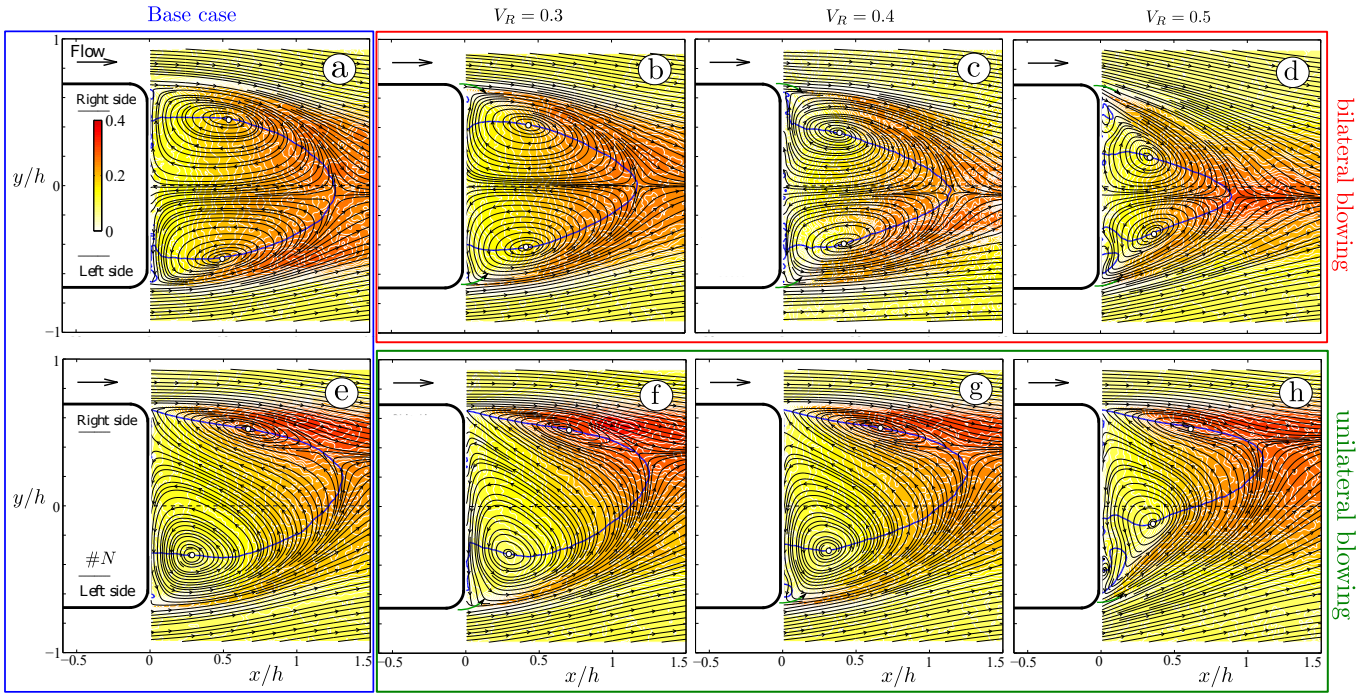

FIG. (5) Time-averaged streamline fields of steady blowing configurations (injection angle of $\theta_j = 45°$) with free stream. Contours represent RMS levels. Mean flows of (a) the baseline case, the bilateral blowing cases for (b) $V_R = 0.3$, (c) $V_R = 0.4$, (d) $V_R = 0.5$, and (e) the baseline case conditional average $\#N$. Mean flows of the left-hand side blowing cases for (f) $V_R = 0.3$, (g) $V_R = 0.4$, (h) $V_R = 0.5$. Vortex core locations are denoted by circle symbols.

is remarkable. It shows that the position of the recirculating cores is directly related to their vorticity strength of recirculating cores. This is expected and consistent with recent studies[23,27], which shed light on the role of the free shear layers from the separation in the shape of the recirculation bubble. Lorite-Díez *et al.*[23] proposed a model in which the recirculation length L_r results from an equilibrium between the entrainment velocity that tends to shorten the recirculation and the mass intake that stretches it. Their extensive study explains how the increase of velocity ratio (and flow rate coefficient) forces the wake to undergo successive flow regimes, from *(i)* a mass-driven regime, in which the mass intake from the forcing extends but weakens the recirculation bubble, to *(ii)* a momentum-driven regime, where the entrainment by the shear layers is enhanced by the forcing, and consequently feeds the recirculating cores.

The Coanda effect used in the present study adds the yaw angle θ_j of the converging jets to the complexity of the recirculation mechanism. Non streamwise injection also makes rather ambiguous the estimation of the entrainment velocity because it drastically deviates and deforms the external shear layers. As a result the recirculation bubble is reshaped by this boat-tailing effect and L_r is no longer the only reliable characteristic of the recirculating flow. That is the reason why the monitoring of the vortex cores is preferred to estimating L_r here. Although the locations of vortex cores can be seen as the aftermath of the entrainment and mass injection, they are strongly related to the base drag. Therefore, vortex cores can serve as a reliable indicator characterising the efficiency of the forcing. It comes that the relocation of recirculating vortices further away from the base can be the main objective of flow control strategies aiming to reduce pressure drag.

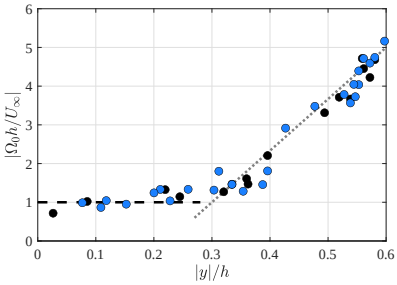

FIG. (6) Absolute value of vorticity, $|\Omega_0 h/U_\infty|$ of the vortex cores as a function of their average spanwise positions, $|y/h|$. Blue and black circles denote the cases of steady blowing at 90° and 45°, respectively.

The averaged positions of vortex cores are plotted in Fig.7 for varying velocity ratios. Both right and left side steady blowing evolve symmetrically, as shown in Fig.7a and 7c, respectively. The wake is gradually more skewed as the main vortex migrates further away from the base and towards the centreline, while the secondary vortex moves upstream and is forced towards its corresponding shear layer. The behaviour is significantly different when bilateral blowing is used (Fig.7b). Symmetric blowing

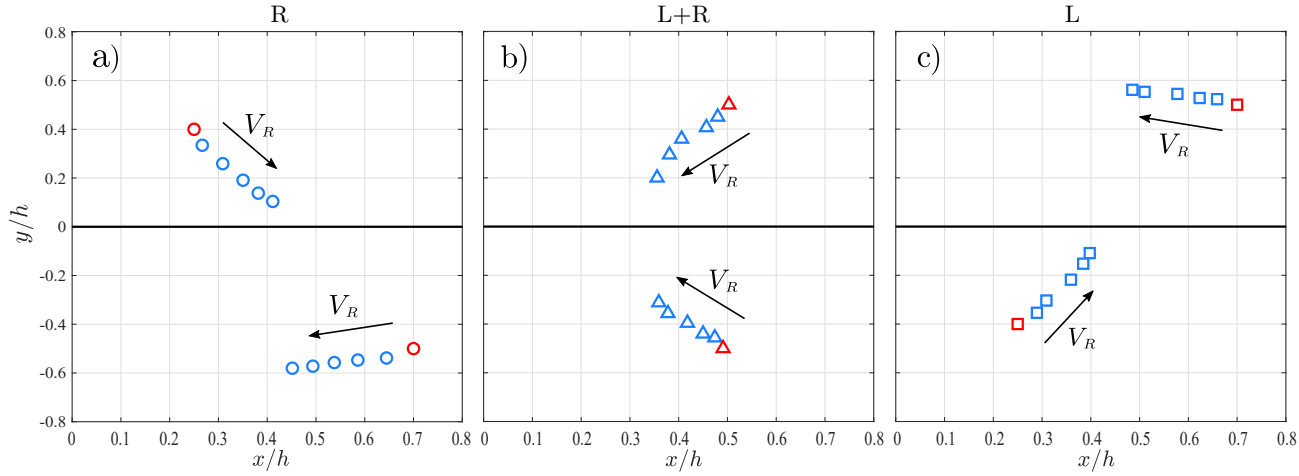

FIG. (7) Vortex core average positions extracted from PIV, for steady blowing (a) on the right-hand side (R), (b) bilateral (L+R), corresponding to FIG.9(a-d), and (c) on the left-hand side (L), corresponding to FIG.9(e-h). Blue symbols denote the position of the vortex cores for $V_R = \{0.3, ..., 0.5\}$ at $\theta_j = 45°$. Red symbols denote the positions of vortex cores $\#N$ and $\#P$ in the reference case $V_R = 0$.

reinforces the symmetry of the wake and shrinks the recirculation region by forcing the two vortex cores closer to the centreline and towards the base. Similar vortex trajectories are observed for a blowing angle of $\theta_j = 90°$ (not reported here for clarity), the forcing is more efficient as its effect kicks in from lower blowing ratios, but vortex trajectories are very similar to those observed at smaller blowing angle.

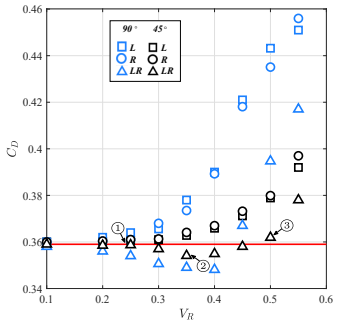

FIG. (8) Drag coefficient as a function the velocity ratio, V_R. The red line denotes the average of the reference case ($V_R = 0$).

B. Drag reduction by convergent steady blowing

The alteration undergone by the recirculation bubble directly affects the pressure distribution of the base and hence, the pressure drag. Direct measurements of the total drag are plotted for all configurations as a function of velocity ratio in FIG.8 for the two injection angles. When one-sided steady blowing is used, drag is systematically increased. The increase is more prominent for the injection angle of $\theta_j = 90°$ than for $\theta_j = 45°$. On the contrary, when the bilateral steady blowing is used (triangle symbols in FIG.8), both injection angles exhibit a global drag reduction for moderate velocity ratios ($V_R < 0.45$). In the case $\theta_j = 90°$, drag reduction occurs directly for the smallest velocity ratio tested. For $\theta_j = 45°$, the best drag reduction is achieved for $V_R \approx 0.35$ while it occurs at $V_R \approx 0.40$ for $\theta_j = 90°$. Bilateral steady blowing with an injection angle of $\theta_j = 0°$ was studied by Lorite-Díez *et al.*[23], who also observed a base drag reduction of 1.1% for a lower blowing velocity ratio of 0.155. The present study is consonant with those results since the base drag reduction is 1.4% for the injection angle of $\theta_j = 45°$ and 3.0% for the case of $\theta_j = 90°$. Besides the deflection of the jets by Coanda effect, it is important to remember that the steady blowing presented in this study uses an air-knife design, with a particularly narrow slit ($h_s/h = 5 \times 10^{-4}$). This constitutes a scenario quite different to most of the other recent works[23–25,32] in which jets were wider or even distributed across an extended area. Note that an extremely focused jet generates a momentum spike, much more intense than the other wider configurations mentioned above. The corresponding mass flow rate might be quite different compared to similar velocity ratios. This aspect will be addressed in future works.

As mentioned earlier, recent works[23,28] have linked the evolution of drag force with blowing intensity to two competing mechanisms impacting the shape of the recirculating region: mass intake and entrainment by the external shear layers. For moderate blowing ratios, the drag decreases as mass intake weakens the recirculating flow while injected momentum remains limited. Above a momentum threshold, the enhanced shear layers driving the vortical cores override the effect of mass intake resulting in a drastic increase of the drag. However the mean flow does not give the full picture when bistability is at play. To better understand the physical mechanisms leading to the change in aerodynamics forces applied to the body due to the forcing, time histories of the side force and drag force coefficients are plotted for an injec-

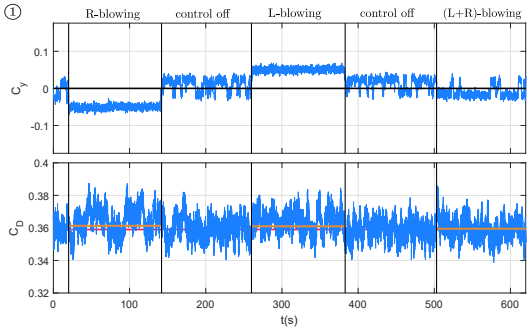

FIG. (9) Time-series of the side force and drag coefficients with various control sequences for $V_R = 0.25$, corresponding to case①. The red line denotes the average of the reference case $V_R = 0$ and the orange line corresponds to the average of the forced cases.

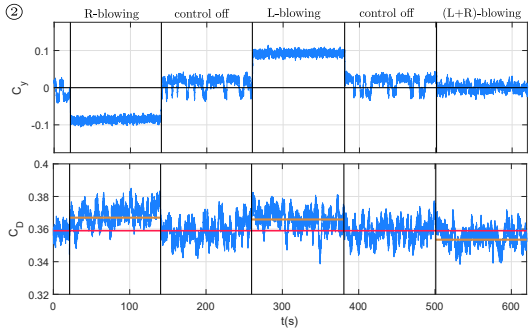

FIG. (10) Time-series of the side force and drag coefficients with various control sequences for $V_R = 0.35$, corresponding to case②.

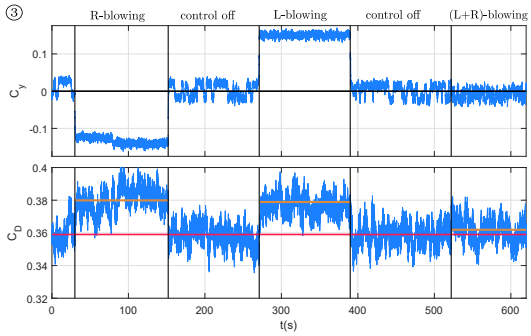

FIG. (11) Time-series of the side force and drag coefficients with various control sequences for $V_R = 0.5$, corresponding to case③.

tion angle of 45°. The use of such time-series generated with the very same aerodynamic balance was recently characterised in an extensive study presented in Lippert *et al.*[29]. Three forcing configurations are considered: one before the drag reduction occurs ($V_R = 0.25$), the second one for the best drag reduction ($V_R = 0.35$) and the last one corresponding to a drag increase ($V_R = 0.5$). These three cases are marked ①, ② and ③, respectively, in Fig.8.

Case ① is plotted in Fig.9. It shows a series of steady blowing phases (R, L and L+R, respectively) separated by no forcing phases. The wake symmetry breaking phenomenon is strikingly exhibited by the natural flow, as expected with this shape ratio w/h and a ground clearance sufficiently high to allow bistability. For this case with a velocity ratio of $V_R = 0.25$, right and left-side blowing cases force the wake to favour asymmetrical $\#N$ or $\#P$ states, respectively. The side-force is kept constant to a higher level than in the natural bistable states, showing the asymmetry is indeed enhanced. As a result, both right and left blowing phases cause an increase of the total drag (orange lines in Fig.9), to be compared to that of the natural case). Bilateral blowing at this low velocity ratio of $V_R = 0.25$ and $\theta_j = 45°$ does not affect the recirculation significantly enough to induce drag reduction. Mass injection and shear layer deviation are too limited at this stage.

Case ② acquired with a velocity ratio $V_R = 0.35$ is depicted in Fig.10, where the same time histories are plotted. Observations for the right and left-hand side blowing phases are similar to the previous case: the enhancement of a constantly skewed wake decreases the fluctuations but leads to significantly higher levels of side force and drag coefficients. The most interesting configuration is when bilateral blowing is used. This case can be compared to the mass regime identified by Lorite-Díez *et al.*[23] as it exhibits a similar drag reduction of 1.5% for a similar velocity ratio. However there is a striking difference in the present case: this regime entails a mitigation of the bistability. Indeed, the side-force coefficient C_y remains close to 0, with little fluctuations, showing that the two asymmetric static modes are strongly dialled down by the forcing. Although bilateral blowing brings the vortex cores slightly closer to the body on average (see §III A), overriding the bistability prevents any vortex from swelling and travelling upstream as observed in skewed states $\#N$ or $\#P$ of the natural flow. The symmetric regime obtained here presents many similarities with the transient regime identified by Haffner *et al* 2020[27] during natural flow reversals. As the entrainment of the vortical cores is equally balanced between the two vortical cores, the recirculation is weakened and base pressure deficits are reduced, resulting in a decrease of the pressure drag. However, contrarily to the transient regime of the naturally bistable flow, this regime is stabilised by the boat-tail reshaping of the recirculation. By deflecting the shear layers inwards, the Coanda effect not only enhances mass intake by the recirculating bubble, it also constrains the extent and the motion of the vortical cores.

Case ③ – with blowing velocity ratio $V_R = 0.5$ – corresponds to an important increase in drag force compared to the natural flow. Time histories of aerodynamic coefficients are shown in Fig.11. Left or right-side blowing configurations exhibit signatures similar to that of cases ① and ② but with drastically multiplied effects. The side force shift is now four times that of the natural bistable case and the drag force has increased by more than 5%. Bilateral forcing becomes sufficiently intense

to switch off the bistability altogether and stabilises a symmetric static mode. However the momentum injected into the shear layers intensifies the entrainment of the recirculating cores, which induces a shortened bubble and counteracts the benefits of a single state without bistability. Another point of interest is the RMS level of C_y and C_D: it is significantly increased compared to case ②, which suggests a more intense volatility of the wake.

C. Base pressure gradients

To analyse further the mechanism leading to drag reduction, the pressure distribution at the base of the body is investigated with respect to blowing velocity. The spanwise and vertical base pressure gradients g_y and g_z are estimated from these pressure distributions. The evolution of g_y and g_z is plotted in FIG.12 as a function of the blowing velocity ratio with deviation $\theta_j = 90°$, for both the one-sided and the bilateral blowing cases. The natural flow is referred to as the reference case in the following. Its bistable state exhibited by the pressure field results in two maxima of the probability density function (PDF) of spanwise gradient $g_y = \pm 0.13$ in FIG.12a. The corresponding maximum of the PDF of the vertical base pressure gradient g_z is equal to 0.058, and is insensitive to the switching dynamics due to ground effects (see FIG.12b), as reported in the literature[28,33]. The associated time-averaged base pressure field is depicted in FIG.12b for future comparison.

The one-sided blowing cases are plotted using left or right conditionally averaged pressure distributions in FIG.12a. The resulting spanwise gradient g_y remains equal to the corresponding skewed mode exhibited by the bistable reference case. The base pressure distributions are indeed reminiscent of the #N state or the #P state, respectively – see FIG.9 for comparison. This confirms that one-sided blowing selects and stabilises a skewed state of the wake quite similar to the corresponding bistable mode in the reference case. The vertical base pressure gradient g_z (FIG.12b) has a positive yet significantly lower value than the reference case. It continues to decrease to reach zero at $V_R = 0.35$.

In §III B the bilateral forcing was shown to reduce bistability until it neutralises it completely above a critical velocity ratio. For $\theta_j = 90°$ this threshold is $V_R = 0.4$. This evolution is saliently depicted by the conditionally averaged spanwise pressure gradients g_y plotted in black lines in FIG.12a. The vertical base pressure gradient g_z continuously decays from the reference case to reach zero at $V_R = 0.4$. and remains null for higher values of V_R. The base pressure field at $V_R = 0.4$ is quite symmetric both spanwise and vertically. This is confirmed by the time series of the base pressure gradients g_y and g_z shown in FIG.12c. It corresponds to the maximum reduction of total drag. When bilateral blowing is increased ($V_R > 0.4$), the flow experiences a new symmetry breaking (FIG.12b). The mean pressure distribution now

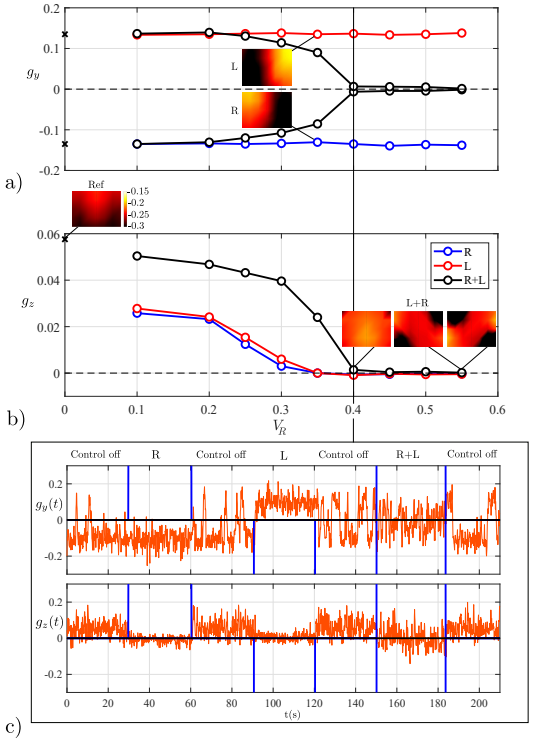

FIG. (12) Sensitivity maps for injection angle of $\theta_j = 90°$, corresponding to the maximum of the probability density functions of the base pressure gradient components (a) g_y and (b) g_z against V_R, along with examples of base pressure distributions; (c) time series of the pressure gradient components for $V_R = 0.4$. Cross symbols denote the reference case without control.

alternates between two quadripolar modes, each presenting a central symmetry. The resulting averaged gradients g_y and g_z remain null but the drag force is drastically increased. Such a reorganisation of the wake is observed for the first time in this context to the authors' knowledge. This new topology is reminiscent of 3D instabilities arising due to jets impinging onto one another. That phenomenon is only encountered for maximal deviation $\theta_j = 90°$ at high velocity ratios, when the boat-tail contraction of the recirculation bubble is extreme.

IV. CONCLUDING REMARKS

Steady inwards blowing was implemented on a square back Ahmed body to manipulate and reshape the recirculation bubble. The impact on the global drag was characterised for a range of blowing strategies, one-sided and bilateral, and associated with the reconfiguration undergone by the wake. Building on recent studies in which streamwise blowing was used, this work introduces a yaw angle to blowing via Coanda effect on air-knife injections from the trailing edges of the body. Depending on velocity ratio and blowing orientation, the adjustment of the wake leads to a variety of flow regimes, most of which being associated with drag increase. Drag reduction is only obtained with bilateral blowing

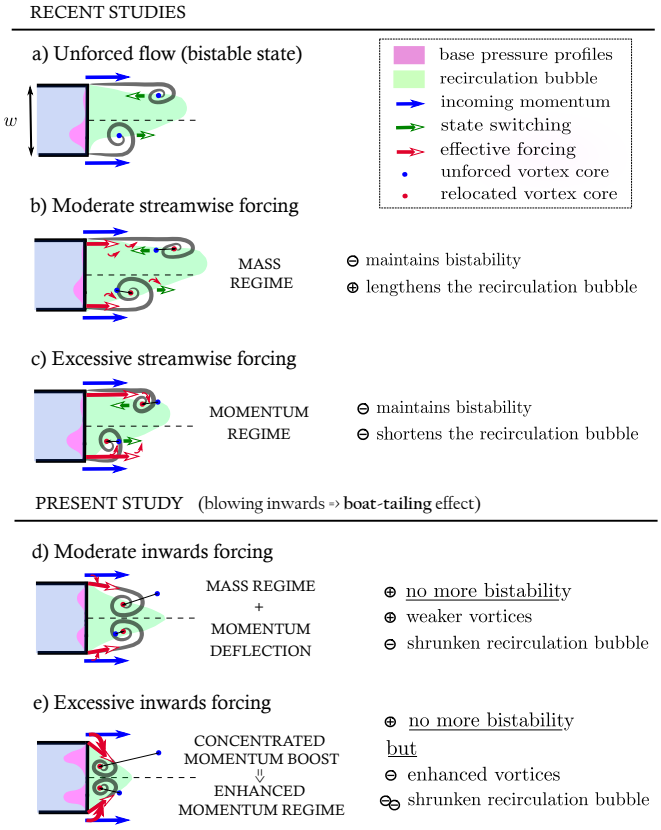

FIG. (13) Organisation of the recirculation bubble and its adjustment operated by air-knife symmetric steady blowing. Compared to literature, notably Lorite-Díez *et al*[23].

and moderate velocity ratios $V_R < 0.45$, but all configurations highlight interesting features of the forced wake.

One-sided blowing cases override the bistability of the natural flow to stabilise around a skewed recirculation bubble resembling the corresponding asymmetric static state of the unforced wake. This was expected from previous studies using asymmetric blowing strategies[23,27,28]. Moreover, the Coanda-deflected steady blowing targets the momentum boost to the neighbouring vortical core. This enhances the asymmetry even further and yields a higher drag force and a side force C_y up to four times that of the bistable states. Note that a range of unbalanced blowing configurations (different velocity ratio on each side) were investigated. The results were showing a gradation of wake asymmetry following the forcing asymmetry. Asymmetric forcing is of particular interest when dealing with realistic flow conditions, that is with a skewed incoming flow. The susceptibility to cross wind in the case of passive control using rear cavities was investigated by Lorite-Díez *et al* 2020[34]. Unlike passive control strategies, two-output active control could offer robust control by asymmetric forcing to compensate cross-wind effects.

Bilateral blowing produces different effects depending on the velocity ratio and deflection angle. The sketches displayed in FIG.13 describe the flow regimes of the recirculation bubble in the present study, and compare them to the known regimes identified in Lorite-Díez *et al* 2020[23]. The evolution of the wake with the velocity ratio shows similar characteristics to streamwise forcing. At moderate velocity ratios, the so-called mass regime in which the recirculation is weakened by the mass injected into the wake, results in a drag reduction up to 3% for $V_R = 0.4$ and $\theta_j = 90°$. When bilateral blowing is increased further, the momentum transferred to the shear layers outweighs the mass regime as it intensifies the recirculating vortical cores. This momentum regime is associated with a significant drag increase and a much shorter recirculation length.

In addition to these competing mechanisms, Coanda-effect targeted forcing brings a boat-tailing effect into play. The use of deflected air-knife blowing has a preponderant impact on the reshaped recirculation bubble. Primarily, inwards blowing constrains the recirculation bubble around a more stable symmetrical static state. The lateral bistable symmetry breaking of the natural flow is tuned down for moderate velocity ratios $V_R < 0.4$. It is neutralised altogether for higher V_R. The boat-tailing contraction due to inwards blowing implies the recirculation bubble is shrunken for all velocity ratios. Targeted momentum injections probably contribute to an increased mass exchange with the shear layers, which intensifies the recirculation. For moderate velocity ratios, this likely limits the drag reduction obtained by cancelling out bistability. For higher momentum cases, the drag increase worsens due to boosted focused vortical cores. Finally, the most intense cases of bilateral blowing ($V_R > 0.5$ and $\theta_j = 90°$) reveal a new bifurcation towards quadripolar modes, resulting from overpowered impinging deflected jets.

ACKNOWLEDGMENTS

The authors are sincerely grateful to the reviewers for their invaluable comments. The review process has greatly improved the quality of the manuscript. This work has been supported by Campus International pour la Sécurité et l'Intermodalité des Transports, Région Nord-Pas-de-Calais, l'Union Européenne, Direction de la Recherche, Enseignement Supérieur, Santé et Technologies de l'Information et de la Communication and le Centre National de la Recherche Scientifique (CNRS).

[1] S. Ahmed, G. Ramm, and G. Faltin, "Some salient features of the time averaged ground vehicle wake," Society of Automotive Engineers. , SAE Inc 840300 (1984).
[2] M. Grandemange, O. Cadot, A. Courbois, V. Herbert, D. Ricot, T. Ruiz, and R. Vigneron, "A study of wake effects on the drag of the ahmed's squareback model at the industrial scale," Journal of Wind Engineering and Industrial Aerodynamics **145**, 282–291 (2015).
[3] T. Castelain, M. Michard, M. Szmigiel, D. Chacaton, and D. Juvé, "Identification of flow classes in the wake of a simpli-

fied truck model depending on the underbody velocity," J. Wind Eng. Ind. Aerod. **175**, 352–363 (2018).
[4]Z. Chen and C.-Y. Wen, "Flow control of a d-shaped bluff body using different dbd plasma actuators," Journal of Fluids and Structures **103**, 103292 (2021).
[5]P. Bearman, "Investigation of the flow behind a two-dimensional model with a blunt trailing edge and fitted with splitter plates," J. Fluid Mech. **21(2)**, 241–255 (1965).
[6]M. Lorite-Díez, J. Jimenez-Gonzalez, C. Gutierrez-Montez, and C. Martinez-Bazan, "Drag reduction of slender blunt-based bodies using optimized rear cavities," Journal of Fluids and Structures. **74**, 158—-177 (2017).
[7]M. Pastoor, L. Henning, B. Noack, R. King, and G. Tadmor, "Feedback shear layer control for bluff body drag reduction," J. Fluid Mech. **608**, 161–196 (2008).
[8]P. Bearman, "The effect of base bleed on the flow behind a two-dimensional model with a blunt trailing edge," Aeronautical Quarterly **18(3)**, 207—-224 (1967).
[9]M. Grandemange, M. Gohlke, and O. Cadot, "Turbulent wake past a three-dimensional blunt body. part 1. global modes and bi-stability," J. Fluid Mech. **772**, 51–84 (2013).
[10]M. Grandemange, M. Gohlke, and O. Cadot, "Turbulent wake past a three-dimensional blunt body. part 2. experimental sensitivity analysis," J. Fluid Mech. **752**, 439–461 (2014).
[11]M. Grandemange, M. Gohlke, and O. Cadot, "Bi-stability in the turbulent wake past parallelepiped bodies with various aspect ratios and wall effects," Phys. Fluids **25(9)**, 095103 (2013).
[12]R. Li, D. Barros, J. Borée, O. Cadot, B.-R. Noack, and L. Cordier, "Feedback control of bimodal wake dynamics," Exp. in Fluids **57**, 158–164 (2016).
[13]B. Plumejeau, S. Delprat, L. Keirsbulck, M. Lippert, and W. Abassi, "Ultra-local model-based control of the square-back ahmed body wake flow," Phys. Fluids **31(8)**, 085103 (2019).
[14]R. Brackston, J. G. de la Cruz, A. Wynn, G. Rigas, and J. Morrison, "Stochastic modelling and feedback control of bistability in a turbulent bluff body wake," J. Fluid Mech. **802**, 726–749 (2016).
[15]P. Gilliéron and A. Kourta, "Aerodynamic drag reduction by vertical splitter plates," Exp. in Fluids **48**, 1–16 (2010).
[16]G. Bonnavion and O. Cadot, "Boat-tail effects on the global wake dynamics of a flatbacked body with rectangular section," Journal of Fluids and Structures. **89**, 61–71 (2019).
[17]J.-M. Lucas, O. Cadot, V. Herbert, S. Parpais, and J. Délery, "A numerical investigation of the asymmetric wake mode of a squareback ahmed body – effect of a base cavity," J. Fluid Mech. **831**, 675–697 (2017).
[18]G. Bonnavion, O. Cadot, V. Herbert, S. Parpais, R. Vigneron, and J. Delery, "Effect of a base cavity on the wake modes of the squareback ahmed body at various ground clearances and application to drag reduction," 23^th French mechanical congress, Lille, France. (September 28-1, 2017).
[19]A. Evrard, O. Cadot, V. H. D. Ricot, R. Vigneron, and J. Délery, "Fluid force and symmetry breaking modes of a 3d bluff body with a base cavity," J. Fluids and structures. **61**, 99–114 (2016).
[20]D. Barros, J. Borée, B. Noack, A. Spohn, and T. Ruiz, "Bluff body drag manipulation using pulsed jets and coanda effect," J. Fluid Mech. **805**, 422–459 (1965).
[21]D. Barros, J. Borée, B.-R. Noack, and A. Spohn, "Resonances in the forced turbulent wake past a 3d blunt body," Phys. Fluids **28**, 065104 (2016).
[22]Y. Haffner, J. Borée, A. Spohn, and T. Castelain, "Unsteady Coanda effect and drag reduction for a turbulent wake," Journal of Fluid Mechanics **899**, A36 (2020).
[23]M. Lorite-Díez, J. I. Jiménez-González, L. Pastur, C. Martínez-Bazán, and O. Cadot, "Experimental analysis of the effect of local base blowing on three-dimensional wake modes," Journal of Fluid Mechanics **883**, A53 (2020), publisher: Cambridge University Press.
[24]T. I. Khan, A. R. Tajik, and V. Parezanovic, "Drag reduction of a generic transport vehicle model using a fluidic oscillator," International Journal of Thermofluids **15**, 100180 (2022).
[25]D. Veerasamy, A. R. Tajik, L. Pastur, and V. Parezanović, "Effect of base blowing by a large-scale fluidic oscillator on the bistable wake behind a flat-back Ahmed body," Physics of Fluids **34**, 035115 (2022), publisher: American Institute of Physics.
[26]E.-C. Hsu, L. Pastur, O. Cadot, and V. Parezanović, "A fundamental link between steady asymmetry and separation length in the wake of a 3D square-back body," Experiments in Fluids **62**, 95 (2021).
[27]Y. Haffner, J. Borée, A. Spohn, and T. Castelain, "Mechanics of bluff body drag reduction during transient near-wake reversals," Journal of Fluid Mechanics **894**, A14 (2020).
[28]Y. Haffner, T. Castelain, J. Borée, and A. Spohn, "Manipulation of three-dimensional asymmetries of a turbulent wake for drag reduction," Journal of Fluid Mechanics **912**, A6 (2021).
[29]M. Lippert, J. Basley, and L. Keirsbulck, "On the reliability of aerodynamic balance time-series for closed-loop flow control," Measurement , 111953 (2022).
[30]C. Chovet, M. Feingesicht, B. Plumjeau, M. Lippert, L. Keirsbulck, F. Kerhervé, A. Polyakov, J.-P. Richard, W. Abassi, and J.-M. Foucaut, "Sliding mode control applied to a square-back Ahmed body," European Journal of Mechanics-B/Fluids **81**, 151–164 (2020), publisher: Elsevier.
[31]L. Graftieaux, M. Michard, and N. Grosjean, "Combining piv, pod and vortex identification algorithms for the study of unsteady turbulent swirling flows," Meas. Sci. Technol. **12**, 1422–1429 (2001).
[32]T. I. Khan, V. Parezanović, L. Pastur, and O. Cadot, "Suppression of the wake steady asymmetry of an Ahmed body by central base bleed," Physical Review Fluids **7**, 083902 (2022), publisher: American Physical Society.
[33]G. Bonnavion and O. Cadot, "Unstable wake dynamics of rectangular flat-backed bluff bodies with inclination and ground proximity," J. Fluid Mech. **854**, 196–232 (2018).
[34]M. Lorite-Díez, J. I. Jiménez-González, L. Pastur, O. Cadot, and C. Martínez-Bazán, "Drag reduction on a three-dimensional blunt body with different rear cavities under cross-wind conditions," Journal of Wind Engineering and Industrial Aerodynamics **200**, 104145 (2020).